remote sensing

Article

Research on the Characteristics of Thermosyphon Embankment Damage and Permafrost Distribution Based on Ground-Penetrating Radar: A Case Study of the Qinghai–Tibet Highway

Shunshun Qi [1,2,3], Guoyu Li [1,2,3], Dun Chen [1,2,3,*], Fujun Niu [1,4], Zhizhong Sun [1,2,3], Gang Wu [1,2,3], Qingsong Du [1,2,3], Mingtang Chai [5], Yapeng Cao [1,2,3] and Jianwei Yue [6]

1 State Key Laboratory of Frozen Soil Engineering, Northwest Institute of Eco-Environment and Resources, Chinese Academy of Sciences, Lanzhou 730000, China; qishunshun@nieer.ac.cn (S.Q.); guoyuli@lzb.ac.cn (G.L.); niufj@scut.edu.cn (F.N.); sun@lzb.ac.cn (Z.S.); wugang@lzb.ac.cn (G.W.); xbdqs@lzb.ac.cn (Q.D.); caoyapeng@lzb.ac.cn (Y.C.)
2 University of Chinese Academy of Sciences, Beijing 100049, China
3 Da Xing'anling Observation and Research Station of Frozen-Ground Engineering and Environment, Northwest Institute of Eco-Environment and Resources, Chinese Academy of Sciences, Jagdaqi 165002, China
4 South China Institution of Geotechnical Engineering, School of Civil Engineering and Transportation, South China University of Technology, Guangzhou 510640, China
5 School of Civil and Hydraulic Engineering, Ningxia University, Yinchuan 750014, China; chaimingtang@nxu.edu.cn
6 School of Civil Engineering and Architecture, Henan University, Kaifeng 475001, China; yjw@vip.henu.edu.cn
* Correspondence: chendun@lzb.ac.cn

Abstract: In order to research the special embankment (thermosyphon embankment) damages and the distribution of permafrost under the Qinghai–Tibet Highway (QTH) embankment. The section K2952–K2953, which is a typical representative of the QTH, was chosen for the detection and research of the permafrost and embankment damages in order to determine the sources of the damages. In this study, the performance characteristics of the embankment, the active layer, and the permafrost table found in ground-penetrating radar (GPR) images were researched, combined with multi-source. According to the research findings, the construction of the embankment in this section has stabilized the effect on the permafrost table. Under the embankment of the unemployed thermosyphon section, the permafrost distribution has good structural integrity and continuity, with the permafrost table at a depth of around 5 m. The continuity of the permafrost distribution under the embankment in the thermosyphon section was poor, and there was localized degradation, with the permafrost table being approximately 6 m deep. The main cause of the irregular settlement and other damage in this section is the presence of a loose area at the base of the embankment. Although the thermosyphon on both sides of the embankment also plays a role in lifting the permafrost table, it is not ideal for managing the damage to high embankments where the type of permafrost under the embankment is high-temperature permafrost with a high ice content and where the sunny–shady slope effect is obvious. The research results described in this article can therefore provide a crucial foundation for the detection of highway damage and permafrost under embankments in permafrost regions in the future.

Keywords: ground-penetrating radar; Qinghai–Tibet highway; permafrost; multi-source data; thermosyphon embankment; embankment damage

Citation: Qi, S.; Li, G.; Chen, D.; Niu, F.; Sun, Z.; Wu, G.; Du, Q.; Chai, M.; Cao, Y.; Yue, J. Research on the Characteristics of Thermosyphon Embankment Damage and Permafrost Distribution Based on Ground-Penetrating Radar: A Case Study of the Qinghai–Tibet Highway. *Remote Sens.* **2023**, *15*, 2651. https://doi.org/10.3390/rs15102651

Academic Editor: Fabio Tosti

Received: 10 April 2023
Revised: 9 May 2023
Accepted: 18 May 2023
Published: 19 May 2023

1. Introduction

Ground that has been below 0 °C for two or more years consecutively is referred to as permafrost [1–3]. It occurs frequently in regions with a high latitude and altitude, including the Arctic, Siberia, and the Qinghai–Tibet Plateau (QTP) [4]. The QTP's permafrost, which covers an area of 1.06 × 10^6 km^2, is the world's largest high-altitude permafrost and makes up around 40.2% of the area there [5,6]. Many linear projects run from north to south through the QTP's permafrost region, which has a harsh ecological environment and complex geological conditions, such as the QTH, the Qinghai–Tibet Railway (QTR), and the Golmud–Lhasa Refined Oil Product Pipeline (GLROPP) [7,8]. The permafrost under the QTH's embankments has changed as a result of the double effects of global warming and human activities, which has made the permafrost's frost heaving and thaw settling an increasingly significant problem for the QTH (Figure 1a,b). Among these, thawing settlement of permafrost under the embankment accounts for 80% of the embankment damage and is strongly correlated with permafrost ice content and the ground temperature [9–12]. A temperature difference between the asphalt pavement and the surroundings as a result of the QTH's asphalt paving has also had an impact on the permafrost under the embankment [13,14]. The stability of the embankment is also impacted by the asymmetric thawing of the permafrost under the embankment brought on by the sunny–shady slope effect [15,16]. As a result, many different types of special embankment, primarily divided into active and passive temperature-controlling measures, have been used on the QTH to mitigate the effects of changes in the permafrost under the embankment [17]. Block-stone embankments, thermosyphon embankments, and duct-ventilated embankments are the three main active temperature-controlling measures, with thermosyphon embankments being the most common on the QTH (Figure 1c–e) [7,17–20]. However, serious damage continues to happen in some areas where thermosyphons have been used [21]. Therefore, with an already damaged thermosyphon embankment, it is necessary to research the damage to the embankment and the permafrost under it.

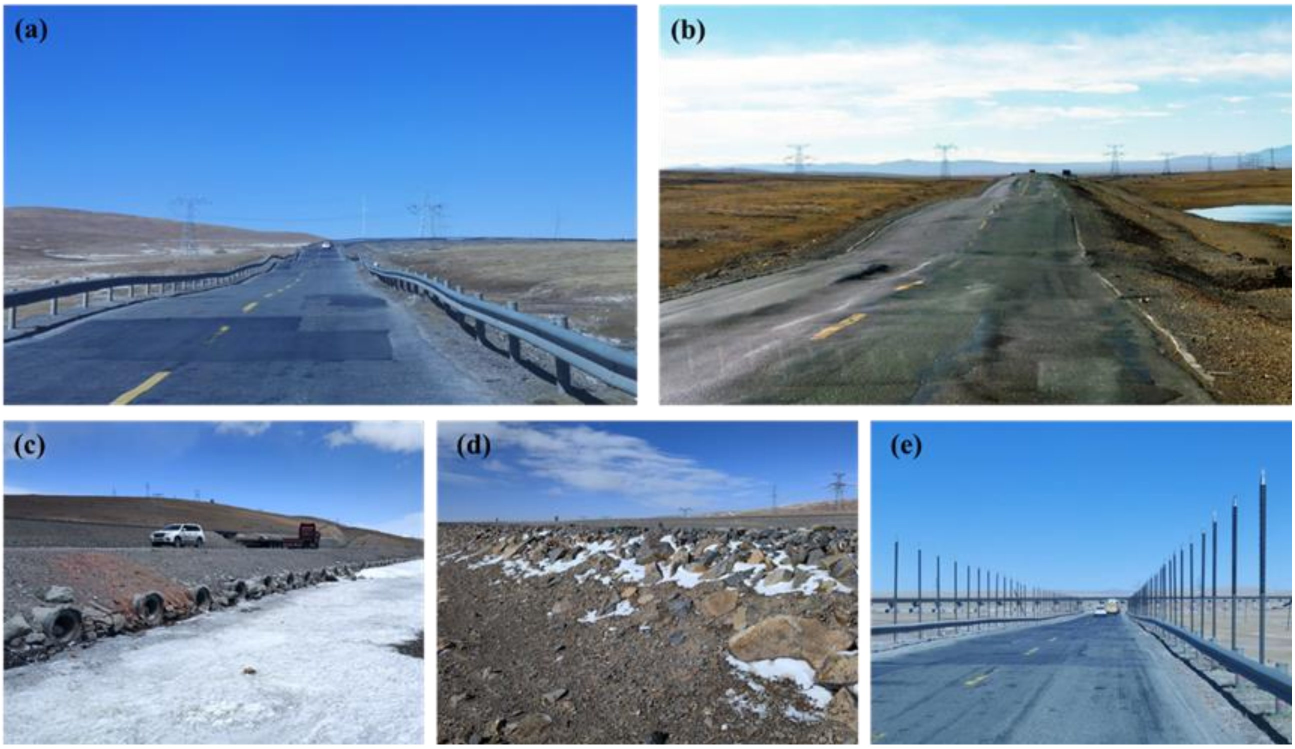

Figure 1. Local photographs of the QTH: (**a**) a photo of repaired pavement; (**b**) a photo showing embankment settlement; (**c**) a duct-ventilated embankment; (**d**) a block-stone embankment; and (**e**) a thermosyphon embankment.

Before the widespread use of new technologies, field surveys were the most basic method of researching the damages to the QTH. However, because surveys are time-consuming and demand a heavy workload, the data obtained are also subject to personal subjective influence, which affects the accuracy of the research results [22]. Furthermore, the survey information, such as the height of the embankment and the type and distribution of pavement damage, is largely superficial. Drilling, which can immediately gather a variety of information on the permafrost and damage, is the most direct method for permafrost and damage detection and research. To reflect changes in the permafrost through variations in the ground temperature and damage to the embankment through embankment deformation, temperature and deformation monitoring equipment can be installed in the borehole [14,16,23–26]. Naturally, this method can be used on natural regions or before buildings are constructed. For instance, it would be exceedingly challenging to gain permission to drill into the QTH, and the monitoring equipment that is already in place was put in the QTH during reconstruction and expansion. Because of their great effectiveness and the benefits of requiring less field effort, mathematical models are now also used in this field research as a result of advancements in computer technology [27–32]. Their drawback is that the simulation's accuracy is heavily reliant on the parameter settings, which are influenced by human factors and the correctness of the data [33,34]. Additionally, there are too many variables that must be taken into account when processing particular boundary regions in mathematical simulations, which cause the findings to deviate from reality. The distribution of permafrost in the boundary region, for instance, is difficult to estimate using many of the models used to assess the distribution and degradation of permafrost in the QTP [35]. Research into local, small-scale permafrost areas has typically not been adopted, but remote sensing is a very useful method for large-scale permafrost research that can create a large-scale permafrost distribution map [4,5,36]. In particular, the use of unmanned aerial vehicle (UAV) technology, which offers an effective and accurate method for research into damage to the QTH, has seen a recent increase in the application of remote sensing techniques to investigations into damage to the QTH [22,37,38]. For example, Chai et al. [22] used field surveys and UAV imagery to research pavement damage in the permafrost zone of the QTH. Valuable data including damage types, damage ratio, pavement roughness, and embankment height were provided for the maintenance of the QTH.

Given the irregular and discontinuous distribution of the permafrost under the embankment and embankment damages, geophysical approaches for detection are suited for long-distance linear projects like the QTH. Depending on their range of applicability and the properties of the discovered object, geophysical methods should be chosen. The high-density resistivity method and GPR are two geophysical techniques that are frequently used in the QTH [39,40]. One of them, GPR, is capable of performing continuous, extensive, long-distance non-destructive testing of targets and is particularly well suited for the QTH [41–43].

This non-destructive characteristic of GPR also determines the breadth of its application, including geotechnical surveys, environmental detection, mineral exploitation, archaeological detection, and military detection, among others [44–48]. GPR is also expanding the boundaries of traditional application sectors. For example, Fediuk et al. [49] demonstrated the viability of using GPR to detect shallow submerged artifacts in addition to land objects when it comes to archaeological discovery. As a result, GPR is frequently used in permafrost regions. It is primarily used to investigate the properties and distribution of permafrost, to learn more about how it has degraded, and to look for engineering damage. For example, Wu et al. [50] found that the permafrost in their study area is distinguished by high ground temperatures and high ice content after using GPR and other data to explore the distribution and internal structure of permafrost in the Honhor Basin, Mongolia, suburbs of Ulaanbaatar. Luo et al. [35] investigated the distribution of and changes in the permafrost in the Xidatan region of the northern QTP using GPR, drilling data, and temperature monitoring data. The results indicated that the permafrost was significantly degraded in this region, and human activities had also played an influential role in permafrost degradation in addition to global warming. Using GPR and resistivity tomography technology, Sjöberg et al. [51] estimated the base and table of the permafrost in peatlands in northern Sweden. As a result of the findings, the range of permafrost could be clearly identified and provided data support for future research. A GPR survey of the

China–Russia crude oil pipeline's permafrost section enabled Wang et al. [52] to clearly determine the state of its thawing settlement. Based on the results, only slight settlement occurred when protective measures were in place, and the topographic conditions clearly affected the thawing settlement of pipelines. For the first time, Zeng et al. [41] used GPR in conjunction with the direct current method and drilling. Several typical sections of the QTH were investigated with relative success to determine the distribution of permafrost and variation in an artificial upper depth under the embankment, which provided a valuable guide for future research. Several studies have demonstrated the feasibility of and application prospects for using GPR to detect and research permafrost under embankments and the damage to embankments.

This paper proposes a method for studying thermosyphon embankment damages and underlying permafrost on QTH using GPR and combining multi-source data (borehole data, ground temperature data, field survey data, etc.). In a previous article [7], the damages of the block-stone embankment of QTH were studied using GPR, which may be based more on the structural characteristics of the embankment and the classification of the damages based on the performance characteristics of different layers on the GPR images. In this paper, however, the study of the thermosyphon embankment damages and permafrost under the embankment is more combined with multi-source data, and the relationship between embankment damages and permafrost is also actively explored. According to that, the focus is on the delineation of different layers and the identification of abnormal areas within the embankment. On the basis of this information, the permafrost table under the embankment is located and its distribution characteristics are determined, and, the formation of embankment damages, especially the relationship between the damages and permafrost, is initially discussed. For highway damage detection in permafrost regions, the research results can provide theoretical and technical support.

2. Study Area

2.1. Physical Geography of the Study Area

The Qinghai–Tibet engineering corridor extends from Golmud in the north to Lhasa in the south, with an average altitude of over 4500 m and a total length of about 1120 km, with nearly half of its length located in the permafrost region. Multiple factors affect linear projects in permafrost regions, such as the QTH, QTR, and GLROPP, all of which suffer different degrees of damage, which seriously affects their normal operations [53,54].

The research object for this study was the K2952–K2953 section of the QTH, which is located in the Qingshui River section of the QTH (Figure 2). With an average altitude of 4474 m, it is in a semi-arid climate zone in the sub-cold region of the plateau, with an average annual temperature of −4.5 to −5.0 °C. The highest extreme temperature in the warm season is 20.4 °C, while the extreme temperatures in the cold season can reach about −35 °C. The annual average precipitation is 511.1 mm; the annual evaporation is 1127.4 mm; the annual average for sunshine hours is 2651.2 h; the annual average relative humidity is 67%; the annual average wind speed is 2.89 m/s; and the average ground temperature is 0 to −1 °C. The thermokarst lakes on either side of the highway are developed, and more developed surface vegetation cover is present [21,54,55]. Previous exploration data have indicated that the bedrock layer is made up of extensively weathered mudstone and marl, which is found 1–2 m below the natural surface in gravel soil and 2–8 m below it in gravel sub-clay, and the permafrost table is 2–3 m below the surface of the earth. The permafrost type under the embankment in this section is icy permafrost, which is an ice layer with little soil at a certain depth. This section is classified as sub-stable according to the stability of the entire QTH, and its permafrost engineering conditions are extremely poor.

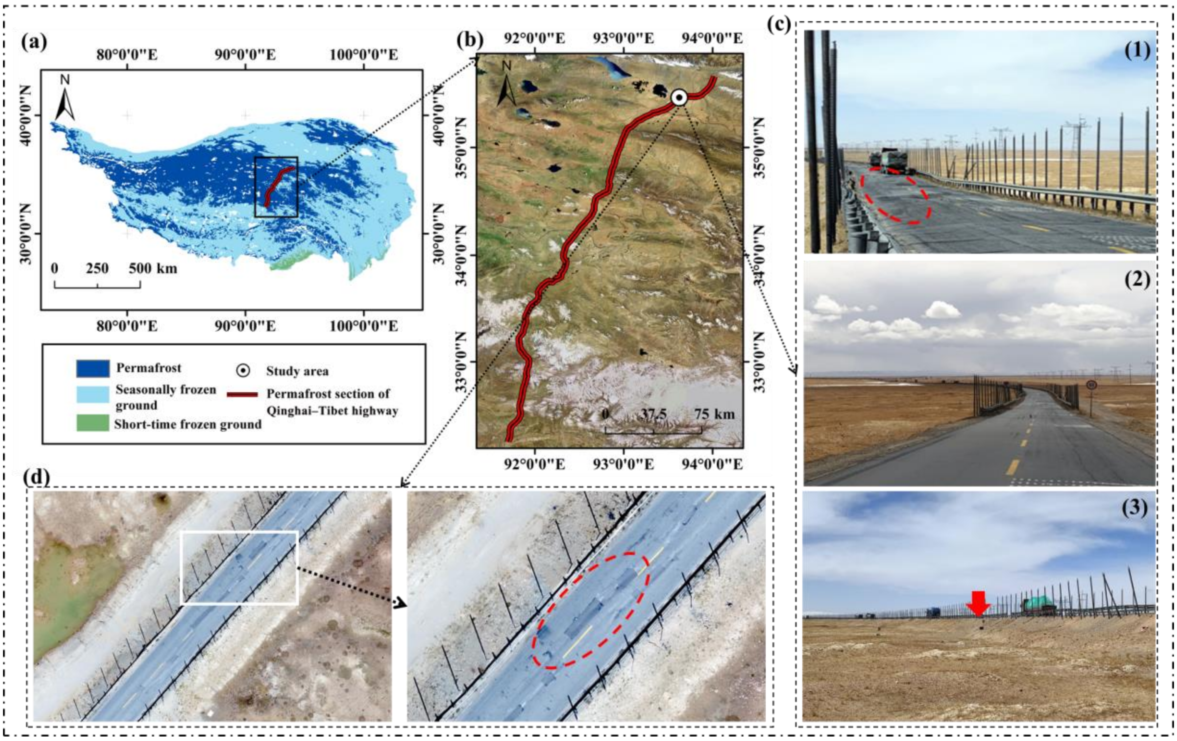

Figure 2. Study area: (**a**) distribution map of permafrost on the QTP [5,56]; (**b**) location of the QTH and the study area; (**c**) field photographs of the study area: (1) severely damaged thermosyphon embankment section; (2) non-thermosyphon sections with good highway conditions; (3) location of monitoring holes and monitoring profile; (**d**) aerial photograph and partial enlargement of the study section (the dark green area on the left side of the embankment is a thermokarst lake). The red dotted line refers to the damaged area, and the red arrow refers to the location of the observation hole.

The QTH is a national secondary highway, and the embankment portion is primarily a filler embankment. The whole highway is asphalt pavement, which can be broken down into the surface layer, base layer, and embankment filler from top to bottom. This section's embankment is classified as a high embankment because of its height, which ranges from 3 to 5 m depending on the topography. High topography, a low embankment, a smooth pavement, and no obvious damage can be found in the first part. In the latter half, the topography is low, the embankment is high, the pavement damage is severe, the repair markings are clear, proactive temperature-controlling measures for thermosyphons are installed on both sides of the highway, and temperature monitoring equipment is located at K2952 + 690. Therefore, we chose this section of the QTH for our research because it is very typical.

2.2. Thermosyphon Embankment

2.2.1. Structure and Working Principle of Thermosyphon

The thermosyphon embankment is a special embankment used to cool permafrost through the continuous transfer of heat from the permafrost under the embankment to the air through the process of evaporation and the condensation of the heat transfer medium in the thermosyphon. Figure 3a depicts the thermosyphon's basic structural elements, including the base tube, the heat transfer medium, the heat sink, and the temperature measuring device. Moreover, the entire thermosyphon can be divided into sections for condensation, adiabatic flow, and evaporation. In addition, the thermosyphon can be inserted straight or diagonally into the shoulder of the embankment or at the foot of the slope (Figure 3b) [18].

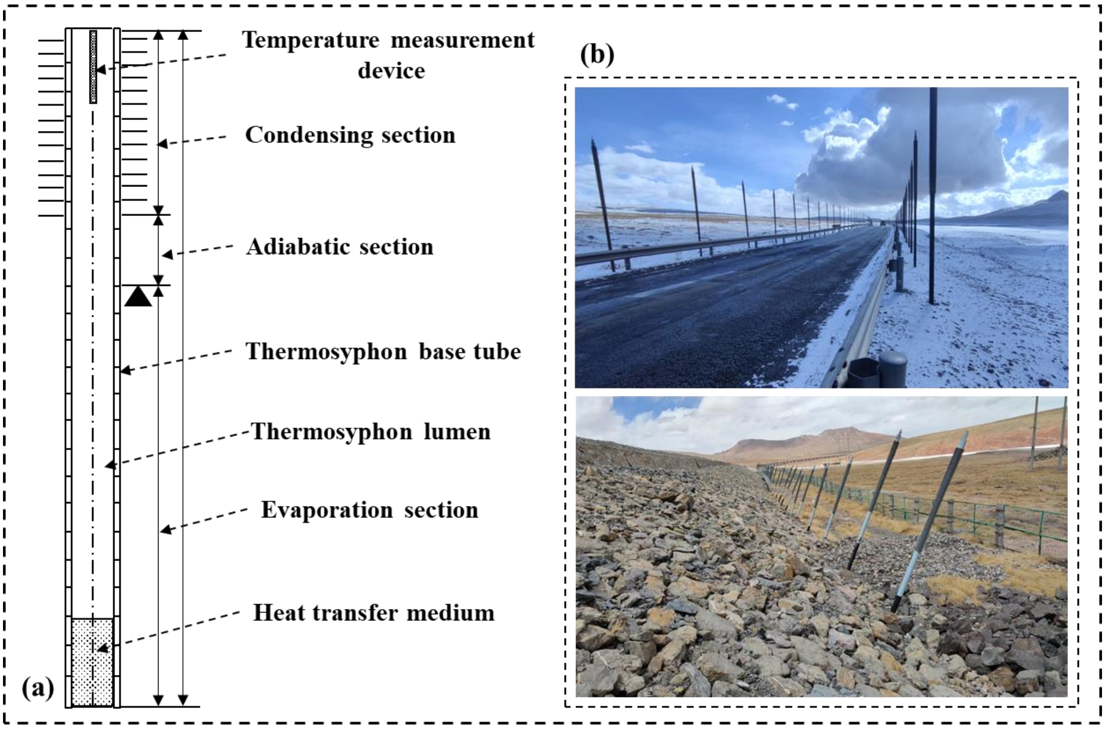

Figure 3. (**a**) Schematic diagram of the structure of the thermosyphon [18]; (**b**) different ways of installing thermosyphon [7].

Thermosyphons must be discussed separately because they exhibit varied operating conditions depending on the season because they primarily use the temperature differential between the condensing and evaporating sections for heat transmission. Figure 4 shows the working principle of the Thermosyphon.

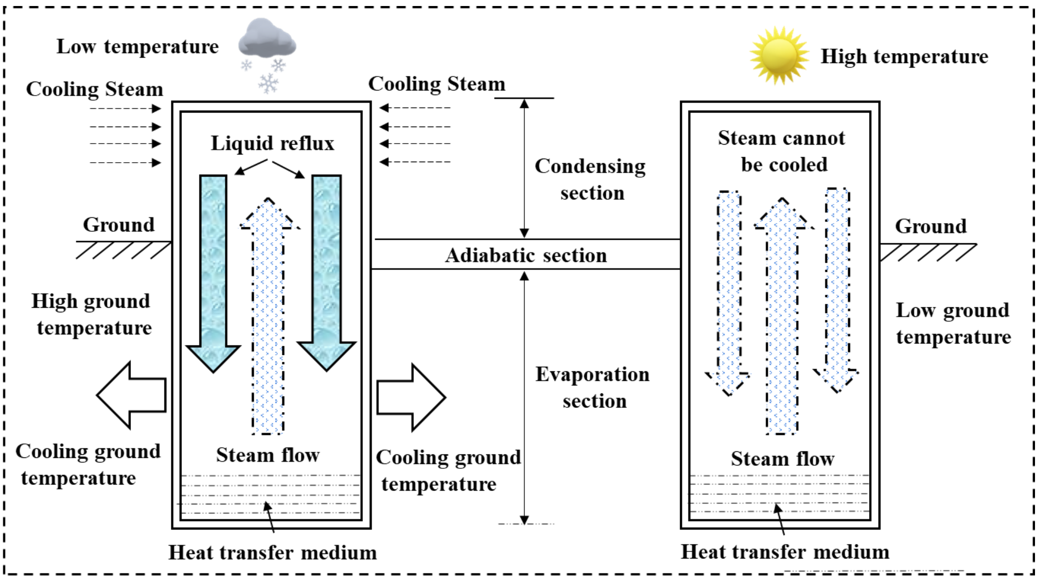

Figure 4. Schematic diagram of the working principle of thermosyphon [18].

The heat transfer medium at the bottom of the thermosyphon is heated and evaporates into steam during the cold season when the ground temperature of the permafrost at the lower end of the thermosyphon is higher than the air temperature at the upper end of the thermosyphon. The steam then rises to the condensing section. The cold air outside the thermosyphon cools the steam in the condensing section, forming liquid beads that, when gravity takes over, run back along the tube wall to the evaporation section. The heat of the permafrost under the embankment is continuously distributed and brought to the atmosphere through the thermosyphon's evaporation and cooling cycle of the heat transfer medium. As a result, the ground temperature of the permafrost under the embankment is lowered until the temperature at the thermosyphon's two ends is equal, at which point the thermosyphon will cease to function [18,21].

When the permafrost ground temperature at the lower end of the thermosyphon is warmer than the air temperature at the upper end of the thermosyphon during the warm season, the steam generated at the bottom of the thermosyphon cannot be cooled into liquid beads at the upper part of the thermosyphon, making it impossible to generate two relative flow cycles of steam and liquid. As a result, no heat exchange can be created. The thermosyphon, which can only transmit heat from the ground to the air and not from the air to the ground, is a one-way heat transfer device [18,21].

2.2.2. Damage Characteristics of Thermosyphon Embankment

It is necessary to discuss the damages of the thermosyphon embankment with single-sided and double-sided thermosyphons separately because the damage characteristics of the thermosyphon embankment are closely related to the form of laying thermosyphon on both sides of the embankment and the local cooling characteristics of the thermosyphons.

When only one side of the embankment is equipped with thermosyphon, the side equipped with thermosyphon is relatively stable under the cooling effect of the thermosyphon. However, if there are no thermosyphons on one side of the embankment, the permafrost will degrade, causing the side of the embankment to sink. This phenomenon is more common in the QTH permafrost section with thermosyphons on one side. Another type of damage is longitudinal road surface cracking, which mainly affects the side where thermosyphons are employed. This is because the permafrost under the embankment that is inside the thermosyphon's effective cooling radius is relatively stable, whereas the embankment that is outside of this radius will sink and develop longitudinal fissures on the side that is closest to the thermosyphon. These fractures come in a variety of sizes and widths, and if they are not promptly corrected, they may allow water to enter the embankment, which could weaken it and cause more severe damages [21].

When thermosyphons are employed on both sides of an embankment, the permafrost under the embankment on both sides is more stable due to the thermosyphons' action, whereas the permafrost under the embankment near the center will degrade, causing the embankment to also settle, at which point continuous longitudinal cracks will appear on the pavement near both sides of the thermosyphons [21].

3. Data and Methods

3.1. Theory on the GPR

Ultra-high frequency electromagnetic waves are used in GPR, an effective, non-destructive detecting method, to find the distribution of subsurface medium. Through the transmitting antenna, electromagnetic waves penetrate the subsurface where they are reflected and refracted by the medium, which has various physical parameters (dielectric constant, electrical conductivity, and magnetic permeability). A GPR profile is created using the characteristics of the electromagnetic wave signals that are reflected and refracted, and this profile is then analyzed to identify the subsurface medium [57,58].

During GPR detection, the electromagnetic wave will encounter many layers such as the embankment, the active layer, and permafrost. Because the materials that make up these layers have different dielectric constants, electromagnetic waves penetrate through them with different strengths of reflection. The reflection coefficient R expresses the strength of the reflection, and the calculation formula is as follows:

$$R = \frac{\sqrt{\varepsilon_1} - \sqrt{\varepsilon_2}}{\sqrt{\varepsilon_1} + \sqrt{\varepsilon_2}} \tag{1}$$

where ε_1 and ε_2 are the dielectric constants of the medium. The reflection coefficient shows that when the difference in the dielectric constant between the upper and lower layers of the medium is greater, the reflected wave amplitude at the interface is greater, the reflection is more obvious, and it can be seen more clearly on the GPR profile [59]. Additionally, the electromagnetic wave's phase change at the two interfaces can be reflected in both the positive and negative values of the reflection coefficient. For example, when an electromagnetic wave enters the permafrost from the active layer, the active layer's dielectric constant is usually greater than that of the permafrost (R is a positive value), and the phase of the interface reflection wave is the same as the incident wave, and vice versa.

It is evident from the reflection coefficient that the bigger the difference in dielectric constant, the more pronounced the reflection will be because there are significant differences in the dielectric constants of water ($\varepsilon = 81$), ice ($\varepsilon = 3.2$), air ($\varepsilon = 1$), soil ($\varepsilon = 5$–40), and permafrost ($\varepsilon = 3.8$–7.4; the higher the ice content, the lower the dielectric constant) [60]. As a result, the permafrost table under the embankment and some airborne damages in the embankment (such as loose areas, voids, etc.) can be seen more clearly on the GPR image.

3.2. Data Acquisition

3.2.1. GPR Data Collection

The XPRT Crossover CO730 two-dimensional GPR (Impulse Radar, Malå, Sweden) was used to detect the permafrost section of the QTH in October 2020 in order to determine the distribution of the permafrost under the embankment (Figure 5).

(a) **(b)**

Figure 5. Diagram of the field GPR survey on the QTH: (**a**) the GPR survey system; (**b**) the safety vehicle.

The permafrost under the QTH embankment reaches its maximum melting depth in October to November, and QTP has cold weather in November; thus, we chose the month of October, when the climate is generally favorable to conduct GPR detection. Additionally, water in the water-rich areas at the top of the active layer and the bottom of the embankment migrates away over time as the permafrost thaws to its maximum depth, reducing the interference of water with GPR signals. This makes it easier to identify the loose areas brought on by water enrichment.

One survey could simultaneously collect data at two frequencies, 300 MHz (noise reduction antenna) and 70 MHz, using the XPRT Crossover CO730 GPR shielded two-frequency transceiver antennas. The GPR parameter settings are listed in Table 1. Furthermore, the technician used GPS for positioning and meticulously noted any elements that would interfere with the GPR signal during the data collection procedure, such as, highway damage, passing vehicles, and guardrails on the highway.

Table 1. Parameter setting of GPR [7].

Division	Parameter A	Parameter B
Antenna frequency (MHz)	300	70
Antenna spacing (m)	0.23	0.6
Time window (ns)	93	375
Sampling rate (m)	0.05	0.05
Sampling point	300	300
Trigger device	Wheel	Wheel

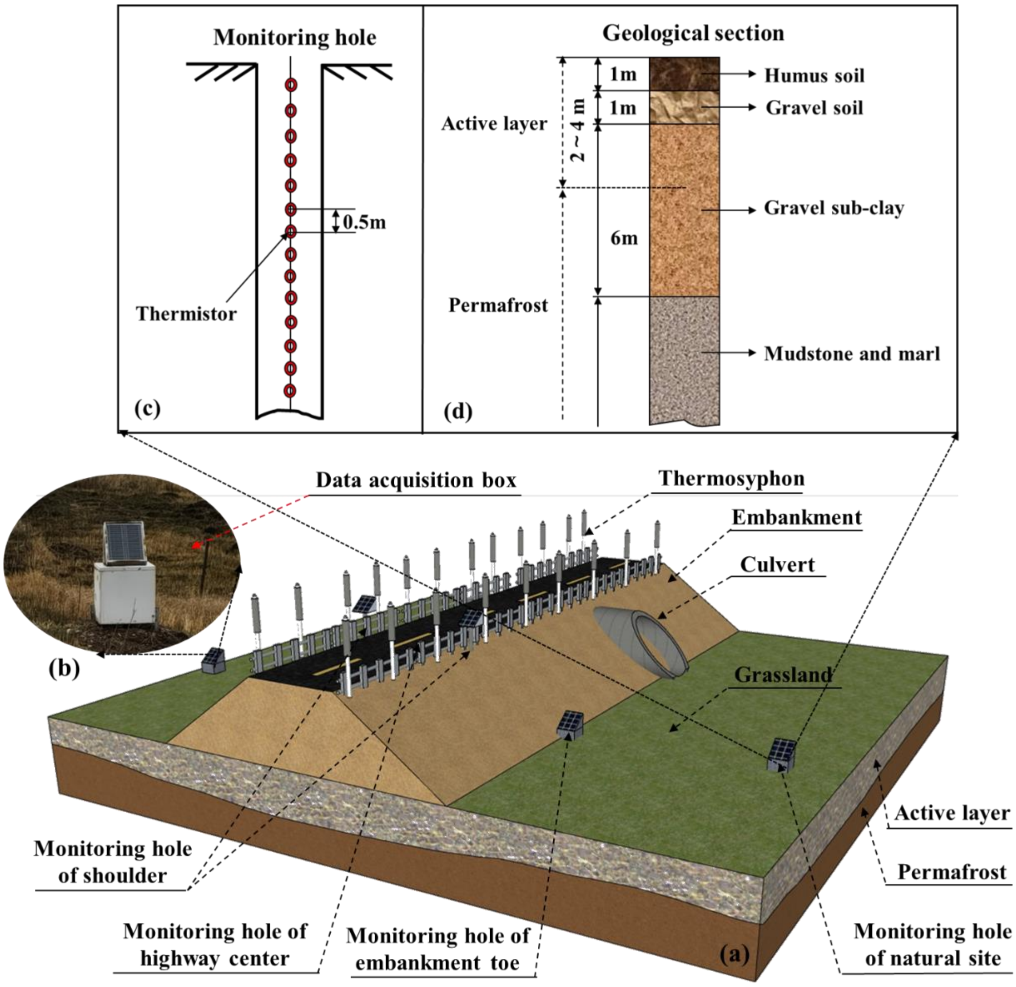

Figure 6. The information related to this monitoring profile: (**a**) typical layout of a ground temperature monitoring profile on the Qinghai–Tibet Highway; (**b**) field photograph of the data acquisition box (including the solar panel); (**c**) schematic diagram of the distribution of thermistors in the borehole; (**d**) geological section of natural site borehole.

3.2.2. Ground Temperature Data Acquisition

The temperature monitoring profile of QTH K2947 + 700 (35°27.747′N, 93°37.747′E) was employed in this study, and it contains five observation holes (natural site, left embankment toe, left shoulder, highway center, and right shoulder). Following the expansion and reconstruction of the QTH, it is now located near the K2952 + 690 section. Figure 6 shows the information related to the monitoring points of this monitoring profile. Temperature monitoring was achieved by converting the resistance values recorded by thermistors (developed by the State Key State Key Laboratory of Frozen Soil Engineering, Chinese Academy of Sciences, with a measurement accuracy of ±0.05 °C) installed in the boreholes into temperatures by means of the corresponding formulae [14,35]. In this temperature monitoring program, the highway center observation hole, the left shoulder observation hole, the right shoulder observation hole, and the natural site observation hole are installed at 0.5 m intervals at depths of 1.2–20.7 m, 0.3–18.3 m, 0.3–14.8 m, and 0.7–15.2 m, respectively. The CR3000 data-logger was powered by a solar panel and a rechargeable battery, allowing it to automatically record the ground temperature data at regular intervals [35].

3.2.3. Other Data Acquisition

We also gathered geological survey data in the research area in addition to the GPR and ground temperature data, as explained in Section 2. Additionally, we thoroughly documented the fundamental state of the embankment and pavement during the field examination, and we obtained infrared images using the Testo-885 thermal infrared camera (Figure 7). The thermal infrared photographs in Figure 7 show that there is a temperature difference between the asphalt pavement and both the embankment and the natural site, which also indicates that the construction of the QTH has changed the local heat exchange conditions.

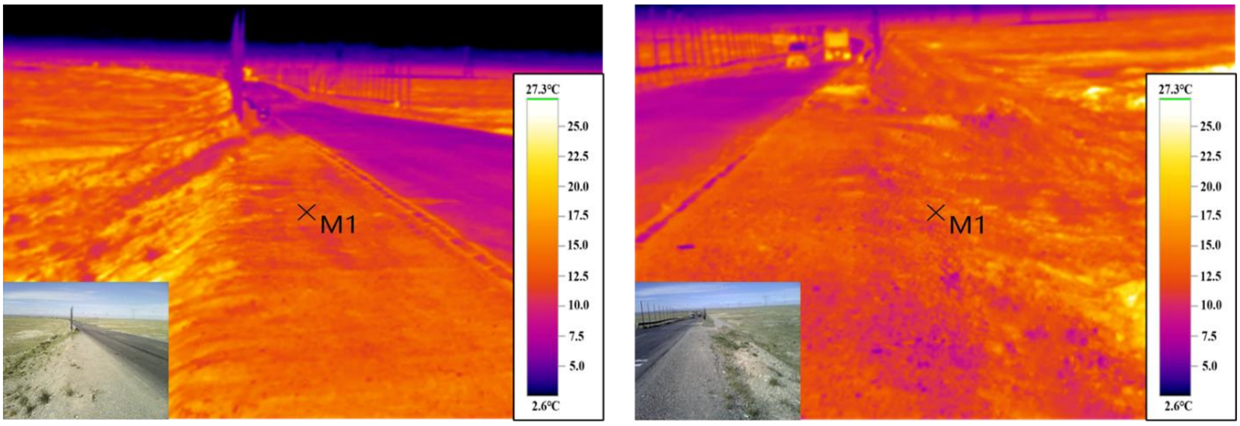

(a) (b)

Figure 7. Local thermal infrared photographs of the K2952–K2953 section of the QTH: (**a**) sunny slope; (**b**) shady slope.

3.3. GPR Data Processing and Presentation

ReflexW software (Sandmeier Geophysical Research, Karlsruhe, Germany) was used to process the GPR data in this study [61]. Data preprocessing and subsequent processing were the major steps in the process. The data processing steps are as follows [59,61,62]:

(1) Arrange the pertinent data (including GPR data, pertinent data captured during the site survey, monitoring data, etc.), import GPR data, and assess the overall state of the data.

(2) Remove direct waves (static correction), and artificially shift observation start time. Due to the intrinsic characteristics of GPR, a portion of direct waves will appear on the GPR images in the raw data gathered in the field. In order to determine the precise time at which electromagnetic waves actually enter the ground, we must remove this portion of direct waves.

(3) Gain (energy attenuation), which amplifies the deep attenuated signal. Since different medium will attenuate the electromagnetic wave, the amplitude will also decrease as the electromagnetic wave is attenuated. As a result, energy gain is frequently utilized in data processing to boost the deep signal's amplitude.

(4) Use two-dimensional filtering (average path extraction) to remove the excess horizontal signal from the GPR image. After gain processing, the electromagnetic wave's amplitude gain in the depth direction might exceed expectations, making the original horizontal signal more obvious. To remove the extra horizontal signal, background removal means are required.

(5) Use one-dimensional filtering (Butterworth bandpass filtering) to eliminate low-frequency parts of the signal, making useful signals clearer and clearer.

(6) Use two-dimensional filtering (moving average) to suppress noise and make the image smooth and clear. When GPR data are processed using a variety of methods, the discrete nature of the data is strengthened and the fluctuations in adjacent data increase. Sliding average processing is needed to remove these fluctuations.

The aforementioned steps are the standard processes in data processing; however, different methods must be selected for unique situations. For instance, inverse fold processing is required to remove the "Ringing" effect and increase vertical resolution. In order to achieve the best processing outcomes, it is therefore important to choose the right processing steps and methodologies based on the quality of the data.

The processed radar data are displayed as two-dimensional images, where the horizontal axis corresponds to the highway mileage scale, the left vertical axis displays the electromagnetic signal's two-way travel time, and the right vertical axis converts time to depth using a velocity of 0.11 m/ns. GPR images at 300 MHz and 70 MHz are simultaneously presented for the same highway section to provide a more thorough presentation of the profile information.

3.4. Methodology

This research makes an attempt to identify the causes of thermosyphon embankment damage as well as the permafrost distribution characteristics under the embankment. The research idea is to use information from diverse sources to determine the region of embankment damage and the distribution range of permafrost under the embankment, and then use that information to investigate the causes of embankment damage and the effect of thermosyphon embankment on permafrost.

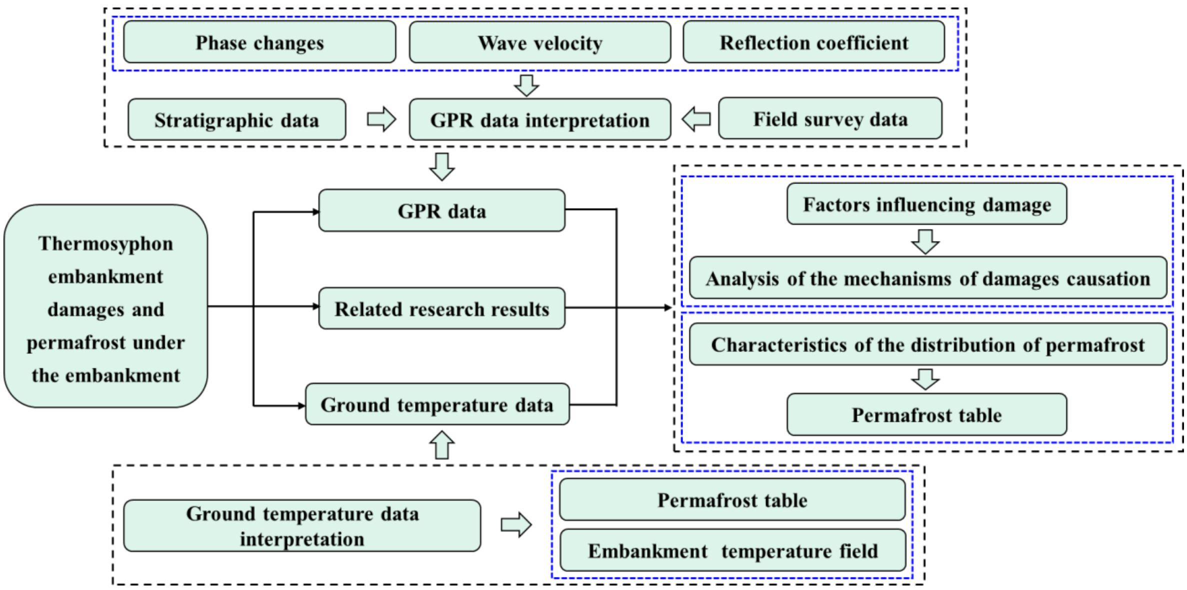

Figure 8. Research routes flow chart. The black line segments and arrows indicate the flow and the wide green arrows indicate the derivative relationships. The black dotted box and the blue dotted box act as a boundary.

Figure 8 shows the research route's flow chart. For our analysis and study, GPR data are used as the primary source, supplemented by multi-source data, and they are combined with these data. To create images that can be used for data interpretation, the GPR data are gathered and processed in a variety of ways. The interpretation of GPR images is based on wave velocity analysis, reflection coefficients (reflection intensity), and phase changes, and for areas with high water content, signal attenuation is also taken into account. The multi-source data mainly includes the following: ground temperature data, stratigraphic data, and field survey data. Where the ground temperature data allow the depth of thawing of the permafrost to be obtained for different periods and thus the permafrost table to be deduced for different periods. In addition, the temperature field in and around the embankment can be constructed from the ground temperature. The determined stratigraphic information can serve as a reference for stratigraphic stratification on GPR profiles; the on-site measured embankment height can be used as the foundation for separating embankment and natural surface; and the damage state of the highway can serve as a crucial foundation for the local abnormal GPR signal interpretation. The environment surrounding the embankment should also be carefully recorded, notably the water accumulation on both sides of the highway, which results in local water-rich areas in the active layers and the embankment. In addition, the results of earlier studies might be used as a guide when interpreting targets, particularly where there is a dearth of information or disagreement on targets.

4. Results

4.1. Ground Temperature Data

Ground temperature changes have the greatest impact on permafrost, but they also reflect permafrost changes. Figure 9 shows the ground temperature variation trends for the natural site, the left shoulder, the highway center, and the right shoulder from 2002 to 2020 for the monitoring profile K2952 + 690. The change in the ground temperature was used to reflect the change in permafrost.

As shown in Figure 9a, the natural site's ground temperature is increasing year by year, while the depth of the maximum melting is decreasing year by year, indicating that the natural site's permafrost table is decreasing and that there is significant degradation of the permafrost. Figure 9b shows that the left shoulder monitoring hole's maximum melting depth from 2002 to 2020 steadily decreased and then stabilized at a depth of around 5–6 m. It can be seen from Figure 9c that the depth of the maximum melting remained at a depth of around 6 m after a gradual rise from 2002 to 2020, indicating that the effects of constructing the QTH on the permafrost has reached a steady state. Figure 9d shows that, aside from temperature variations in the two earliest years, the maximum melting depth in the right shoulder monitoring hole remained constant at a depth of 3–4 m for the following years. In addition, the proactive temperature-controlling measures of the thermosyphons on the section have had some effect.

In addition, the ground temperature trends of this monitoring profile over the past 20 years, as shown in Figure 9b–d, demonstrate that the ground temperature fluctuated in these three monitoring holes in the early years before becoming stable. This was because the Qinghai–Tibet Highway reconstruction project in 2002 disturbed the ground temperature under the embankment. The subsequent stabilization of the ground temperature also indicates that the thermosyphons employed for this section have been effective, and in another sense, it reflects that the construction of this section of the highway has maintained a relatively stable state with respect to the effect of permafrost under the embankment.

Figure 10 shows the ground temperature variations throughout the year at different observation locations in 2020 for the observation profile K2952 + 690. The ground temperature is divided in the diagram using isotherms of different temperature, with the freezing and melting layers separated by the 0 °C isotherm. Figure 10a shows the annual trend of the ground temperature for the monitoring hole of the natural site, which varies with the seasons, with surface temperatures reaching a maximum in September and a minimum in January. The maximum thaw depth for the year of 3.7 m was reached in November, also indicating that the permafrost table at this location is around 3.7 m in November. Figure 10b–d shows the ground temperature trends for the monitoring hole of the left shoulder, the monitoring hole of the highway center, and the monitoring hole of the right shoulder. Although influenced by the construction of the highway, the temperature trends are similar to those of the natural site, with surface temperatures reaching a maximum in

September and a minimum in January. Maximum thaw depths of 4.3 m, 5.8 m, and 3.4 m, respectively, were reached around November in the left shoulder, the highway center, and the right shoulder.

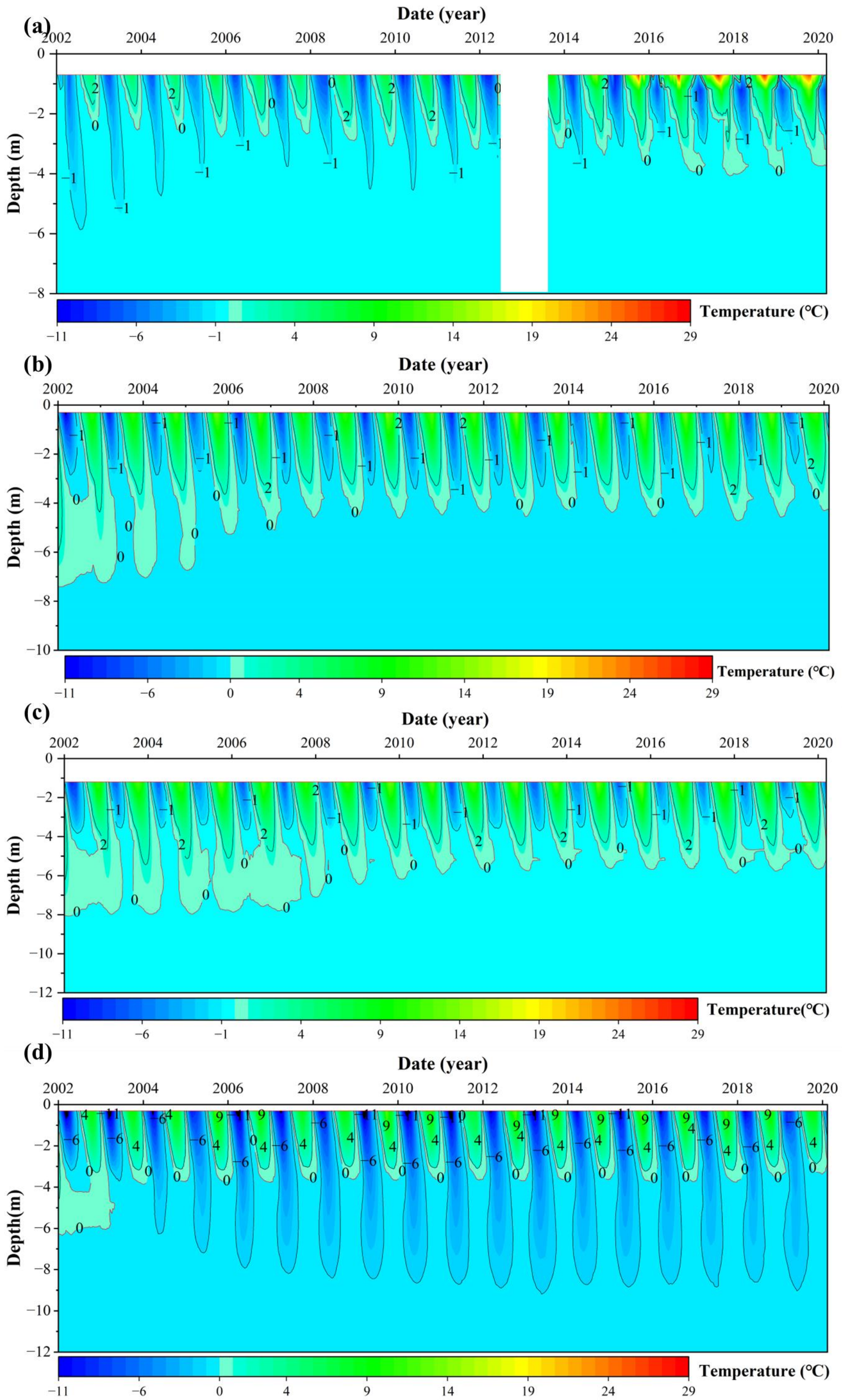

Figure 9. The ground temperature variation trend of the K2952 + 690 monitoring profile from 2002 to 2020: (**a**) monitoring hole of natural site; (**b**) monitoring hole of the left shoulder; (**c**) monitoring hole of the highway center; (**d**) monitoring hole of the right shoulder. Note: The data around 2013 in Figure 9a are missing due to equipment issues.

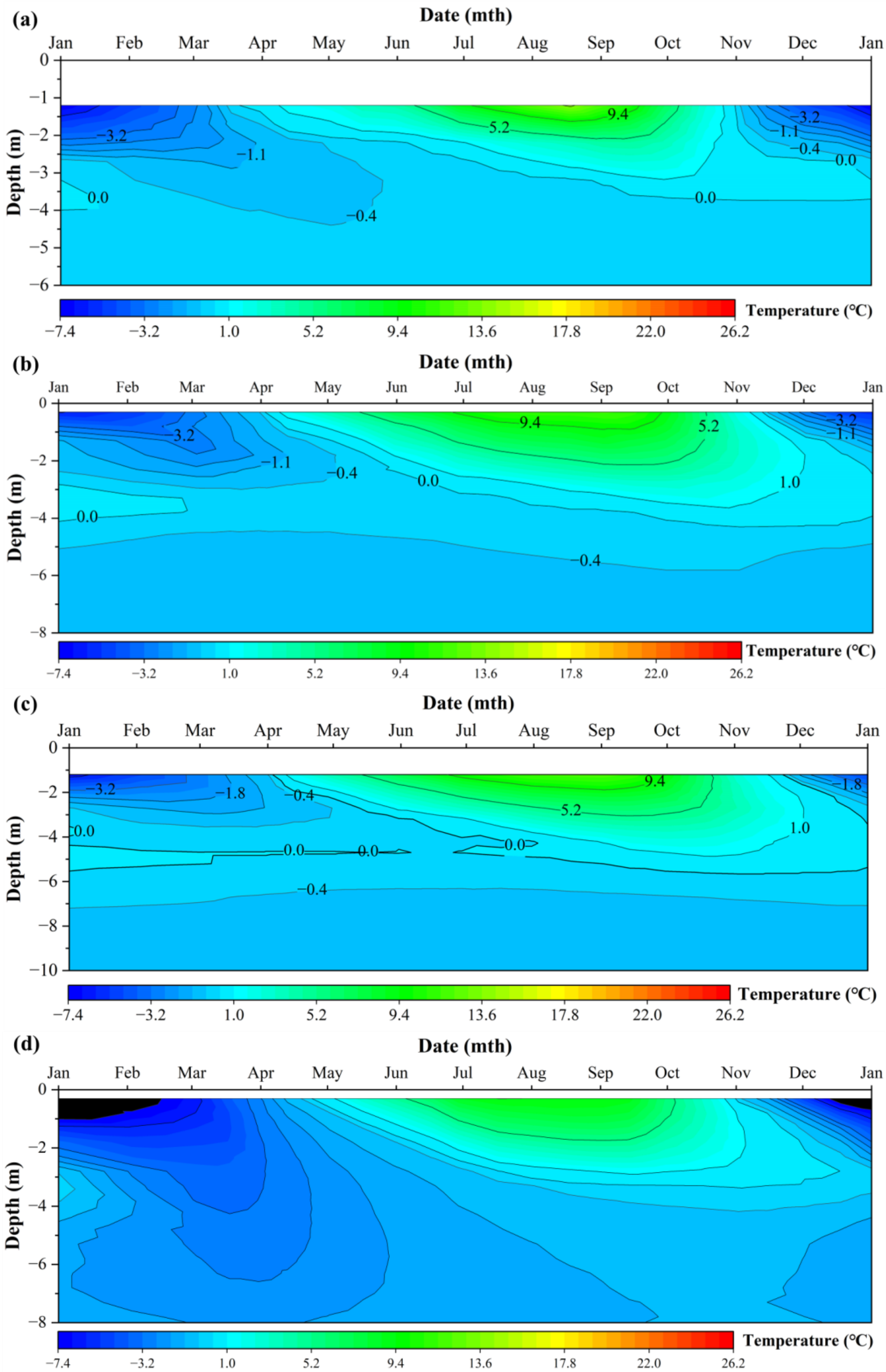

Figure 10. The variation trend of ground temperature in different months of 2020 in the K2952 + 690 monitoring profile: (**a**) monitoring hole of the natural site; (**b**) monitoring hole of the left shoulder; (**c**) monitoring hole of the highway center; (**d**) monitoring hole of the right shoulder. Note: The ground temperature is divided in the diagram using isotherms of different temperatures, with the freezing and melting layers separated by the 0 °C isotherm.

If we compare the ground temperatures of the monitoring holes at different locations in Figure 10, it can be found that the thawing depth at the center of the highway was the greatest during the study period because of factors such as the embankment and the asphalt pavement, and its ground temperature was basically higher than that of the shoulders on both sides of the highway at the same depth range. In addition, a comparison of Figure 10b,d shows that although both the left and right shoulders are cooled by thermosyphons, the difference in the embankment height and the sunny–shady slope effect resulted in the left shoulder being less affected than the right shoulder.

Therefore, from the different types of ground temperature data presented in Figures 9 and 10, we obtained some idea of the distribution and variation of permafrost under the embankment, and could roughly estimate the permafrost table under the embankment at a depth of around 6 m in October on the section near the monitoring hole in the highway center. This information played a very important role in the subsequent interpretation of the GPR data.

4.2. GPR Data

4.2.1. Identification of Permafrost under the Embankments

Because of the obvious variation in highway conditions at different locations in Section K2952–K2953, to make the results representative, a section from the general embankment (without obvious damage, no thermosyphons on either sides, and higher ground; K2952 + 018 to K2952 + 072) and a section from the thermosyphon embankment (with obvious damage, thermosyphons on both sides, and lower ground; K2952 + 643 to K2952 + 697) of the highway were selected. One of the selected sections in the thermosyphon embankment contains the temperature monitoring hole at K2952 + 690, so its GPR data were interpreted first.

Figure 11 shows the GPR image and waveforms at typical locations of the K2952 + 643 to K2952 + 697 section, with the positions of the monitoring hole marked. According to the field investigation, the embankment is around 4 m high, the highway is severely damaged, and there is obvious local settlement of embankment as well as pavement repairs. Figure 11a shows a number of continuous reflections of the in-phase axis, with significant undulations, at depth ranges from 0 to 4.5 m in the GPR profile. A continuous reflection with obvious fluctuations appeared at a depth of about 4 m, which, when combined with electromagnetic characteristics and field survey data, represents the interface between the embankment and the natural ground (marked by the yellow dashed line at the bottom of the image). In addition, there is a strong reflection appeared at a depth of around 3 m (indicated by the yellow dashed box), and the lower part showed a misalignment of the reflection of the in-phase axis, so it was inferred that there is a possibility of localized loosening of the layers in the embankment here. Figure 11b shows cluttered GPR profiles, but it is still possible to see a reflection of the in-phase axis at about 6 m depth with weak continuity, a strong amplitude, and an unchanged phase, so it was inferred from the stratigraphic data (Figure 6d) and the ground temperature data (Figure 10c) that this is the permafrost table under the embankment. In addition, according to the GPR images, the permafrost under the embankment exhibited a discontinuous distribution and differences in the ice content.

Figure 12 shows the GPR image of the K2952 + 018 to K2952 + 072 section. The field investigation showed that the highway surface was smooth and there was no obvious damage. Figure 12a shows several distinct reflections of the in-phase axis in the 0–2 m depth range, with good overall continuity and no obvious fluctuating bending, although there are local misconnections. The height of the embankment investigated on-site had no obvious characteristics at the depth corresponding to this GPR image, and the signal was dominated by low-frequency signals (indicated by the blue dashed box in the waveform diagram in Figure 12a) in the 2–4 m depth range, with no obvious strong reflections, indicating good stratigraphic homogeneity and also indicating that there is no longer a clear boundary between the fill and the active layers at the base of the embankment. Continuous and irregular strong reflections were observed at a depth of 4.5–5 m (indicated by the white arrow); on the basis of their location and the GPR signal's characteristics, it was inferred that they were the permafrost table. The permafrost table under this section of the embankment was inferred from Figure 12b, which shows a clear continuous axis of strong reflection at a depth of around 5 m and shares the same GPR signal characteristics as the permafrost table identified in Figure 11b. Compared with the results in Figure 11b, the permafrost table at this section is higher, with a better continuity of distribution in the subsurface and a higher ice content. Furthermore, compared with the details of the permafrost shown in Figure 12a, Figure 12b shows the profile of the permafrost's distribution; thus, combining the two frequency images can give clearer information. In addition, the interference signals generated by passing vehicles are clearly visible (indicated by the red dashed box).

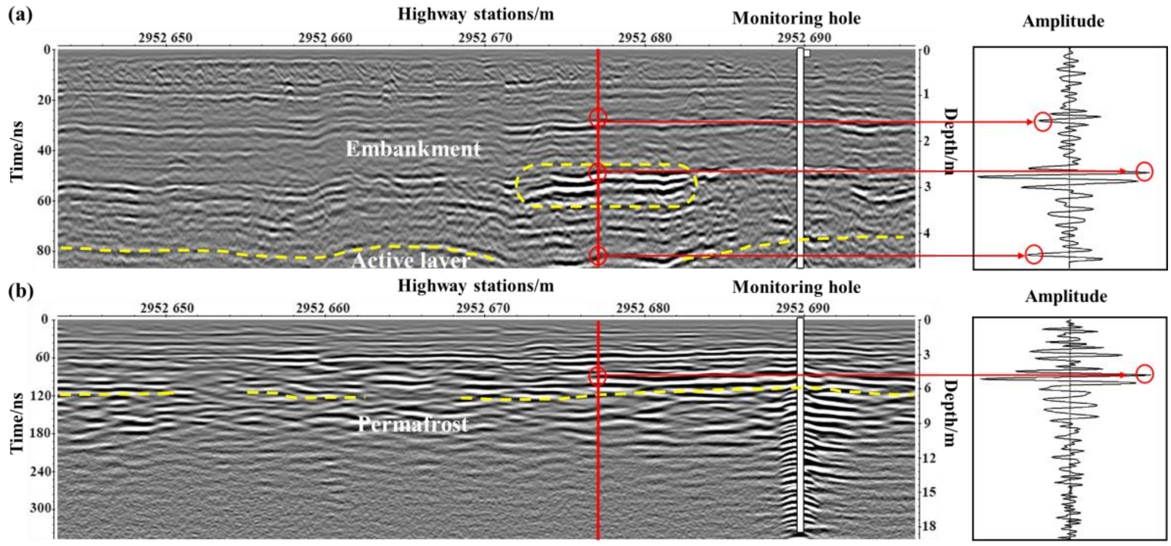

Figure 11. GPR images and waveforms at typical locations of section K2952 + 643 to K2952 + 697: (**a**) 300 MHz; (**b**) 70 MHz. The yellow dotted line is the boundary between different layers; the yellow dashed box represents the strongly reflection area within the embankment.

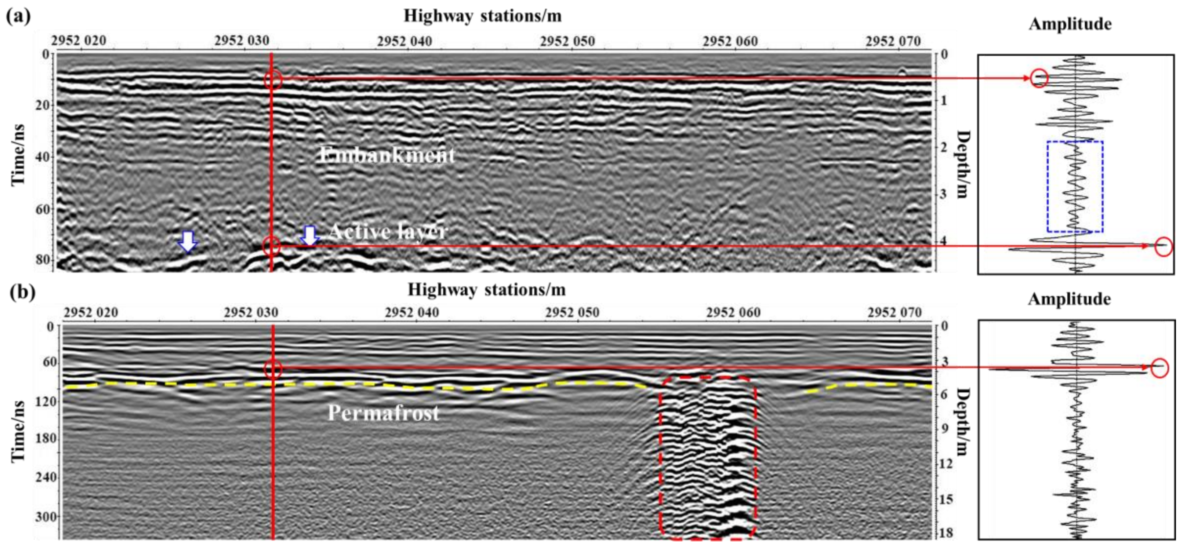

Figure 12. GPR images and waveforms at typical locations of section K2952 + 018 to 1952 + 072: (**a**) 300 MHz; (**b**) 70 MHz. The yellow dotted line is the boundary between different layers, the red dashed box indicates interference signals generated by passing vehicles, and the white arrows indicate the permafrost under the embankment.

4.2.2. Identification of Embankment Damage

The main purpose of researching the permafrost under embankments was to explore the mechanisms and causes of damage to the embankment. Damage to the embankment was also discovered while researching the permafrost under the embankment. In order to conduct research into the damage using the GPR profiles, three sections of the severely damaged section were once again chosen.

Figure 13 shows the GPR profiles of three severely damaged highway sections. The 300 MHz image essentially depicts the entire extent of the embankment because the field survey revealed that the height of the embankments was in the range of 4–4.5 m in these three highway sections. As a whole, the GPR profiles of these three highway sections show significant bending fluctuations and local misalignment of the reflections of the in-phase axis, and a high number of local strong reflections (indicated by the yellow dashed boxes and blue arrows). These GPR image characteristics all suggested the presence of embankment damage, which matched the actual conditions of highway damage.

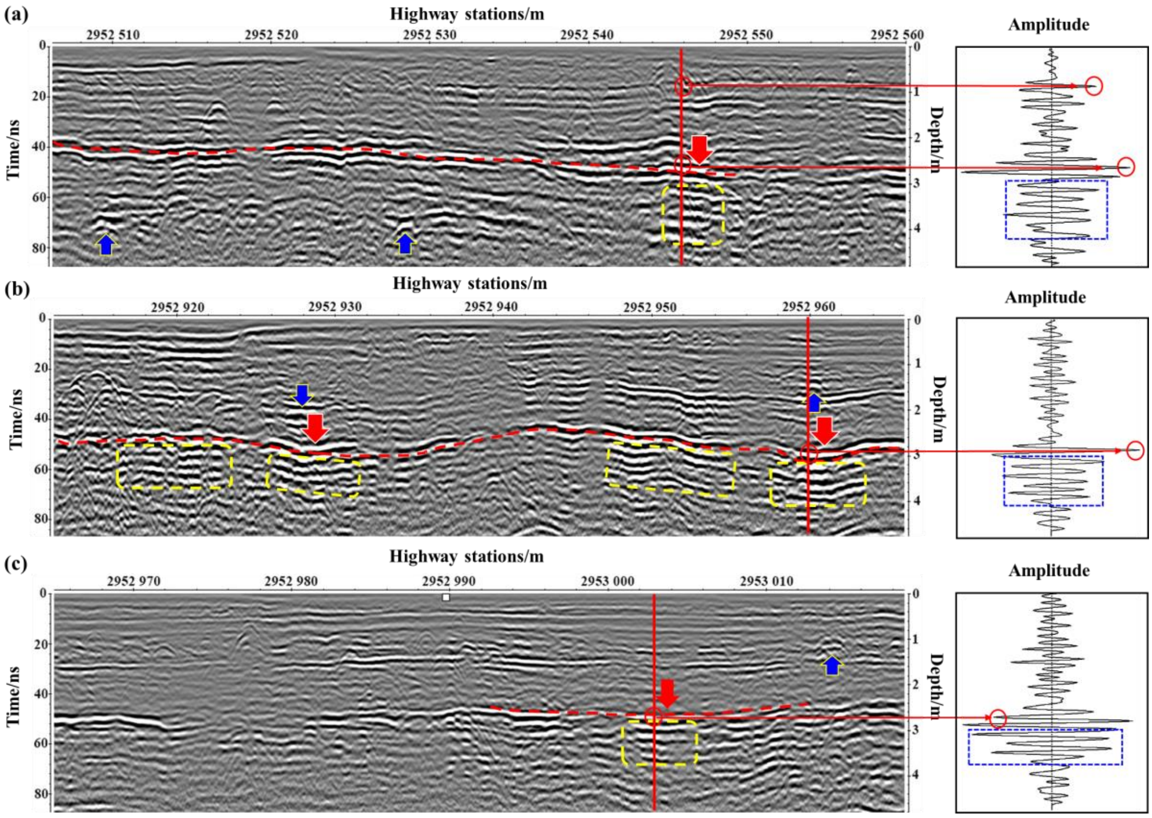

Figure 13. GPR images of 300 MHz and waveforms at typical locations: (**a**) K 2952 + 506 to K2952 + 560; (**b**) K 2952 + 912 to K2952 + 560; (**c**) K2952 + 965 to K2953 + 019. The red dotted line represents the path of the reflections of the in-phase axis, the yellow dashed box represents the loose areas within the embankment, the blue arrows indicate areas of suspected voids within the embankment, and the red arrows shows the settlement trend of the embankment.

Figure 13a–c shows distinct strong reflections of the in-phase axis at a depth of about 3 m (indicated by the red dashed line), along with notable local enhancement and bending fluctuations, which are especially noticeable in Figure 13b. The yellow dashed box indicates where there are more areas of strong reflection. Additionally, in the upper portion of the area where strong reflections exist, the reflections are stronger in the reflections of the in-phase axis, and there is a clear characteristic of local settlement (indicated by the red arrow). The strong reflection areas indicated by the yellow dashed boxes are inferred to be loose areas according to the characteristics present in the GPR images, the electromagnetic wave characteristics (indicated by the blue dashed box in the waveform diagram), and their location. Localized settlement and other damages have resulted from the presence of these loose areas at the base of the embankment, and the settlement of these areas has caused localized layer loosening within the embankment (areas of strong reflections of the in-phase axis). Additionally, voids are suspected within small areas of the embankment (shown by blue arrows), and these voids pose a major safety hazard for the embankment. Therefore, the loose areas within the embankment, combined with the points discussed above, are the main cause of highway damage.

5. Discussion

The permafrost section of the QTH, which is a crucial component of the QTH, has long been plagued by highway damage since its construction. The main causes of embankment damage, in addition to the harsh natural environment of the permafrost area and crushing by large numbers of heavy vehicles [22], are the changes in the permafrost under the embankment, which are closely related to the permafrost table, ice content, and ground temperature [9–12]. Therefore, it is of great significance to detect permafrost under the embankment and embankment damage in the QTH, but it is also difficult and challenging because of the permafrost's irregular and discontinuous distribution. Therefore, this study selected a typical section of the QTH (K2952–K2953) for the detection of and research into permafrost under the embankment and highway damage using non-destructive GPR combined with other information and methods.

5.1. Distribution of Permafrost under the Embankment

The methods used and the conclusions drawn by Zeng et al. [41] in 1993 provided an important reference for this study because they used GPR to detect many areas of permafrost under the embankment in typical sections of the QTH. The distribution of the permafrost under the embankment can be more precisely determined by combining the analysis of the GPR profiles in Figures 11 and 12, the ground temperature picture in Figure 9, and the fact that the permafrost under this embankment is a high ice content permafrost with a low dielectric constant and an obvious GPR reflection between it and the active layer. The results of this study show that the construction of the embankment in this section of the QTH has stabilized the effect on the permafrost table and that the thermosyphons on either side of the embankment have played a role in raising the permafrost table. Furthermore, the distribution of the permafrost table under the embankment in this section changes with the undulations of the terrain, remaining at the depth range of 5–6 m under the embankment.

5.2. Damage Formation and Influencing Factors

5.2.1. Causes of Damage Formation

The damage to the QTH is the consequence of a number of circumstances, and research has indicated that the majority of the existing highway damage is brought on by the embankment's irregular settlement, which is directly related to the degradation of permafrost [11,12]. Significant highway damage exists in the thermosyphon embankment of K2952–K2953, which is also evident in the GPR profile of the embankment, as shown in Figure 13. The embankment shows significant localized settlement and the highway surface has potholes if the reflections of the in-phase axis within the embankment show curvature, dislocation, and discontinuity, and there are obvious areas of localized loosening. When compared with the GPR images shown in Figure 12a, the embankment's integrity is good and there is no obvious damage because the reflections of the in-phase axis within the embankment are continuous and complete with no obvious localized areas of loosening. As a result, the GPR images provide an accurate representation of the damage to the embankment based on the profile characteristics. According to the analysis of Figure 12, the main reason for the settlement damage in this section is the presence of loose areas within the embankment.

5.2.2. Factors Influencing Damage

Thermosyphons are widely used as an active cooling measure on the QTH and have shown promising results [20,21]. Despite the fact that the thermosyphons were buried in the embankment on both sides, the highway suffered severe damage in the research section. Based on the findings above, we have drawn the preliminary conclusion that the main reason for embankment damages is loose areas within the embankment. The presence of loose areas in the embankment also illustrates localized changes in the strength of the embankment. The degradation of permafrost, the regional cooling characteristics of thermosyphons, the sunny–shady slope effect of high embankments, and the rolling of large trucks are only a few of the elements that contribute to changes in embankment strength. Figure 14 shows a preliminary exploration of the embankment damage formation process.

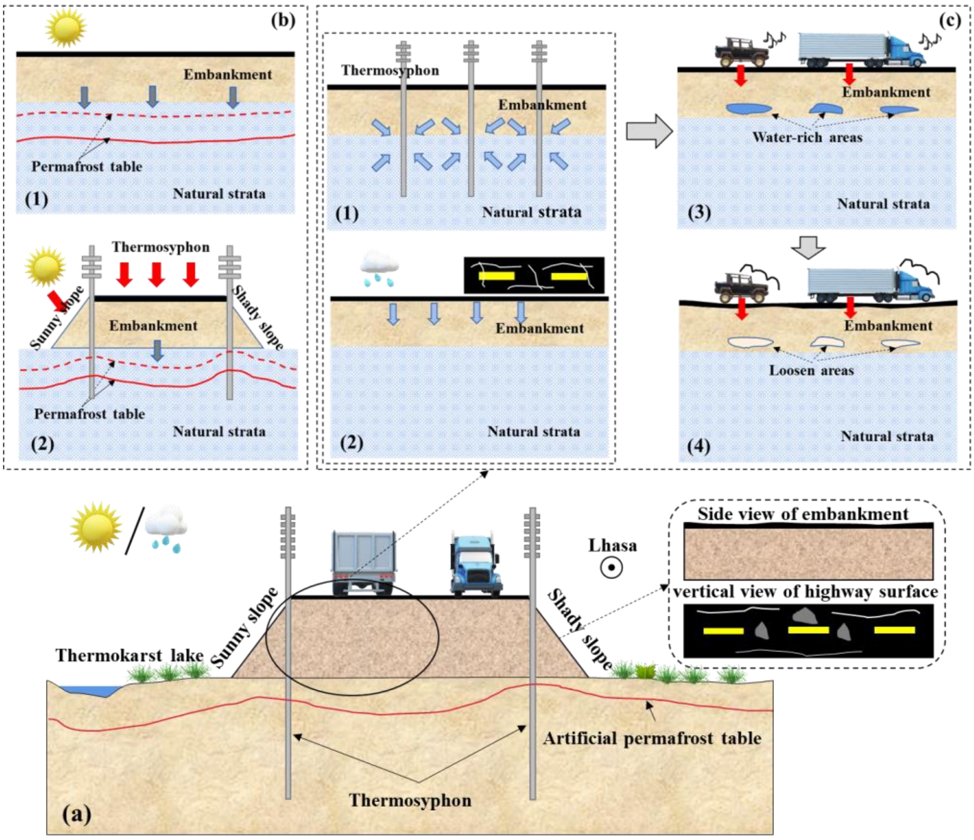

Figure 14. Highway damage formation process: (**a**) representative view of the different orientations of the thermosyphon embankment and its surroundings [21]; (**b**) the effect of permafrost degradation under the embankment on the embankment: (1) influence of permafrost degradation on embankment without thermosyphon. (2) influence of permafrost degradation on embankment during thermosyphon employed. (**c**) effect of thermosyphon employed on embankment: (1) the local cooling characteristics of the thermosyphon cause the moisture in the embankment to migrate around the thermosyphon. (2) longitudinal cracks formed in the pavement after the employed thermosyphons caused water to enter the embankment on the road surface. (3) water-rich areas have formed in the embankment and the embankment has been crushed by vehicles. (4) localized water enrichment leads to a loose and softened embankment and, over the course of time, causes a reduction in the bearing capacity of the embankment, resulting in irregular settlement of the embankment.

Due to the laying of thermosyphons on both sides, the degradation of permafrost here affects the embankment mainly in the uneven degradation of permafrost. The permafrost is relatively stable within the radius of action of the thermosyphon, while the state of the permafrost outside the radius of action is relatively unstable, and the section of the embankment under the permafrost itself has unstable engineering properties of high ice content and high-temperature permafrost, over time, resulting in different strengths within the embankment and an uneven settlement of the embankment (Figure 14b).

The temperature field of the embankment becomes asymmetrical due to the local cooling characteristics of the thermosyphon, causing water to migrate from high-temperature areas to low-temperature areas. As a result, high water content freezing areas form around the thermosyphon, and these areas form obvious local water-rich areas after the warm season thaw. Wang [54] pointed out in his paper that the internal moisture content of the embankment is the highest during the warm season. There will still be some moisture that accumulates in the embankment even if the majority of it will still migrate later. Additionally, the effects of factors such as vehicle crushing, localized frost swelling of the embankment, and freeze–thaw cycle cracking of the embankment cause pavement cracks to form. If these cracks are not repaired in a timely manner, water from the road surface will enter the embankment and create water-rich areas. These local water-rich conditions make the embankment weaker and softer, and the loose area gradually widens as a result of yearly wear and tear and vehicle crushing. This causes the embankment's bearing capacity to be diminished, which leads to irregular settlement of the embankment (Figure 14c).

The sunny–shady slope effect can affect the embankment in addition to permafrost and the thermosyphons. Although both the left and right shoulders are cooled by the thermosyphon, there is still a significant difference in their temperatures, as shown in Figure 10b,d. Asymmetric thawing of the permafrost under both sides of the embankment can be caused by this difference, thus affecting the stability of the embankment. Furthermore, the presence of the thermokarst lakes on both sides of the embankment also influences the melting of the permafrost under the embankment, and the construction of the embankment has accelerated the formation of the thermokarst lakes, forming a vicious circle of mutual influence, which was also reflected in the active layer [54].

5.2.3. Suggestions for Managing Damages

The following suggestions are made for the future construction of thermosyphon embankments in the permafrost regions, accounting for the causes of the damage that has occurred on the thermosyphon embankment in this study. First of all, good embankment drainage is important, especially for high embankments that do not drain well, which can easily lead to water enrichment within the embankment, thus affecting the stability of the embankment. Second, when laying thermosyphons in areas of unstable permafrost with a high ice content, a one-way permeable membrane can be laid on the natural ground surface and at the base of the embankment to prevent moisture migrating from the active layer into the embankment while allowing moisture to drain out. Additionally, the burial density should be adjusted appropriately when laying thermosyphons in accordance with the local geological engineering conditions. In order to stop water penetrating the embankment on the highway surface, cracked lesions on the older pavement should be promptly corrected. Finally, further sunny slope management techniques may be applied concurrently to lessen the effect of the high embankment's sunny slope on the thermosyphon embankment.

5.3. Weaknesses of Current Research

Human error is unavoidable when interpreting the GPR data because the accuracy of data collection and interpretation depends on the technical experience and level of expertise of the researcher. Furthermore, weather and passing vehicles can interfere with data collection. Additionally, the internal structure of the permafrost under the embankment is difficult to detect with the current equipment because of attenuation of the GPR signal caused by the presence of the active layers and the embankment. Therefore, in future research, other geophysical methods could be chosen for detecting the interior of the permafrost that cannot be penetrated by GPR. Additionally, there is a dearth of additional information to support the theory regarding the cause of the embankment damage. When it is not possible to obtain permission to use boreholes for the detection of and research into embankment damage and permafrost under the embankment, the use of GPR in combination with other information is still, of course, the standard option today.

6. Conclusions

This paper draws the following conclusions:

(1) The distribution of permafrost under the embankment in the QTH can be accurately detected using GPR combined with multi-source data. The results show that the distribution of permafrost under the embankment varies with the rise and fall of the terrain, with good continuity and structural integrity in the distribution of permafrost under the embankment in the section K2952 + 018 to K2952 + 072, and the permafrost table is about 5 m in depth. The K2952 + 643 to K2952 + 697 section, where the permafrost table is about 6 m deep, has poor continuity in the distribution of permafrost under the embankment.

(2) It was discovered that the construction of the embankment in this section stabilized the effect on the permafrost table and that the thermosyphons on either side of the embankment contributed to the lifting of the permafrost table, according to the combined GPR data and ground temperature data.

(3) GPR can be used to predict embankment damage in advance and interpret its mechanisms. The findings of this study indicate that there were obvious local loose areas at the bottom of the embankment, which were the main cause of the irregular settlement and other damage in this section of the embankment, and that the influencing factors are multiple.

(4) Thermosyphons have a limited effect on the management of damage to high embankments where the type of permafrost under the embankment is high-temperature permafrost with a high ice content and where the sunny–shady slope effect is obvious, as the sunny–shady slope effect of the high embankment reduces the cooling effect of the thermosyphon.

(5) Due to the attenuation of GPR signals by the embankment and the active layer, it is difficult to probe the internal structure of the permafrost under the embankment with the data collected in this paper. Certainly, the research findings of embankment damages and the permafrost table presented in this paper can also serve as a crucial basis for the future detection of highway damages and the permafrost under embankments in permafrost regions.

Author Contributions: Conceptualization, S.Q., G.L., M.C., F.N., Z.S., G.W. and D.C.; methodology, S.Q., M.C. and G.L.; validation, S.Q., G.L., D.C. and Q.D.; formal analysis, S.Q., G.L., D.C., G.W. and Q.D.; investigation, S.Q., G.L., D.C., F.N. and Q.D.; data curation, S.Q., G.L., Z.S. and D.C.; writing—original draft preparation, S.Q. and G.L.; writing—review and editing, S.Q. and G.L.; visualization, S.Q. and G.L.; supervision, D.C., Q.D., G.L., Z.S., M.C., Y.C. and J.Y.; project administration, G.L. and Y.C.; funding acquisition, G.L. All authors have read and agreed to the published version of the manuscript.

Funding: This research was funded by the Second Tibetan Plateau Scientific Expedition and Research Program (No. 2019QZKK0905), the Science and Technology Project of State Grid Corporation of China (Grant No. 5200-202230098A-1-1-ZN), the Foundation of the State Key Laboratory of Frozen Soil Engineering (Nos. SKLFSE-ZY-20, SKLFSE201913, SKLFSE-ZT-202203), and the programme of Gansu Province Science and Technology Foundation for Youths (No. 22JR5RA089).

Data Availability Statement: Not applicable.

Acknowledgments: The data set in Figure 2a is provided by the National Tibetan Plateau Data Center (http://data.tpdc.ac.cn, accessed on 7 October 2020). The authors especially thank Peifeng He and Jing Luo for their field assistance.

Conflicts of Interest: The authors declare no conflict of interest.

References

1. Xu, X.Z.; Wang, J.C.; Zhang, L.X. *Frozen Soil Physics Science*; Science Press: Beijing, China, 2010; pp. 18–38.
2. Elias, S.A. Alaskan North Slope Coastal Tundra. In *Imperiled: The Encyclopedia of Conservation*; Elsevier: Amsterdam, The Netherlands, 2022; pp. 151–168.
3. Short, N.; Brisco, B.; Couture, N.; Pollard, W.; Murnaghan, K.; Budkewitsch, P. A comparison of TerraSAR-X, RADARSAT-2 and ALOS-PALSAR interferometry for monitoring permafrost environments, case study from Herschel Island, Canada. *Remote Sens. Environ.* **2011**, *115*, 3491–3506. [CrossRef]
4. Obu, J.; Westermann, S.; Bartsch, A.; Berdnikov, N.; Christiansen, H.H.; Dashtseren, A.; Delaloye, R.; Elberling, B.; Etzelmüller, B.; Kholodov, A. Northern Hemisphere permafrost map based on TTOP modelling for 2000–2016 at 1 km2 scale. *Earth-Sci. Rev.* **2019**, *193*, 299–316. [CrossRef]
5. Zou, D.; Zhao, L.; Sheng, Y.; Chen, J.; Hu, G.; Wu, T.; Wu, J.; Xie, C.; Wu, X.; Pang, Q.; et al. A new map of permafrost distribution on the Tibetan Plateau. *Cryosphere* **2017**, *11*, 2527–2542. [CrossRef]
6. Wu, Q.; Zhang, Z.; Liu, Y. Long-term thermal effect of asphalt pavement on permafrost under an embankment. *Cold Reg. Sci. Technol.* **2010**, *60*, 221–229. [CrossRef]
7. Qi, S.; Li, G.; Chen, D.; Chai, M.; Zhou, Y.; Du, Q.; Cao, Y.; Tang, L.; Jia, H. Damage Properties of the Block-Stone Embankment in the Qinghai–Tibet Highway Using Ground-Penetrating Radar Imagery. *Remote Sens.* **2022**, *14*, 2950. [CrossRef]
8. Zhang, Z.; Wang, M.; Wu, Z.; Liu, X. Permafrost Deformation Monitoring Along the Qinghai-Tibet Plateau Engineering Corridor Using InSAR Observations with Multi-Sensor SAR Datasets from 1997–2018. *Sensors* **2019**, *19*, 5306. [CrossRef] [PubMed]
9. Biskaborn, B.K.; Smith, S.L.; Noetzli, J.; Matthes, H.; Vieira, G.; Streletskiy, D.A.; Schoeneich, P.; Romanovsky, V.E.; Lewkowicz, A.G.; Abramov, A.; et al. Permafrost is warming at a global scale. *Nat. Commun.* **2019**, *10*, 264. [CrossRef]
10. Smith, S.L.; O'Neill, H.B.; Isaksen, K.; Noetzli, J.; Romanovsky, V.E. The changing thermal state of permafrost. *Nat. Rev. Earth Environ.* **2022**, *3*, 10–23. [CrossRef]
11. Mu, Y.H.; Ma, W.; Niu, F.J.; Liu, G.; Zhang, Q.L. Study on Geotechnical Hazards to Roadway Engineering in Permafrost Regions. *J. Disaster Prev. Mitig. Eng.* **2014**, *34*, 259–267. [CrossRef]
12. Qingbai, W.; Yongzhi, L.; Jianming, Z.; Changjiang, T. A review of recent frozen soil engineering in permafrost regions along Qinghai-Tibet Highway, China. *Permafr. Periglac.* **2002**, *13*, 199–205. [CrossRef]
13. Zhang, Z.; Wu, Q.; Xun, X. Radiation and energy balance characteristics of asphalt pavement in permafrost regions. *Environ. Earth. Sci.* **2016**, *75*, 221. [CrossRef]
14. Yu, F.; Qi, J.; Lai, Y.; Sivasithamparam, N.; Yao, X.; Zhang, M.; Liu, Y.; Wu, G. Typical embankment settlement/heave patterns of the Qinghai–Tibet highway in permafrost regions: Formation and evolution. *Eng. Geol.* **2016**, *214*, 147–156. [CrossRef]
15. Ya-Ling, C.; Sheng, Y.; Ma, W. Study on the effect of the thermal regime differences in roadbed slopes on their thawing features in permafrost regions of Qinghai–Tibetan plateau. *Cold Reg. Sci. Technol.* **2008**, *53*, 334–345. [CrossRef]
16. Luo, X.; Yu, Q.; Ma, Q.; Guo, L. Study on the heat and deformation characteristics of an expressway embankment with shady and sunny slopes in warm and ice-rich permafrost regions. *Transp Geotech.* **2020**, *24*, 100390. [CrossRef]
17. Fan, K. Study on Design and Construction Techniques of Special Subgrade for Permafrost Areas. Master's Thesis, Chang'an University, Xi'an, China, 2009.
18. Fang, J.; Li, D.; Xu, A.; Tong, C. *Application Technology of Special Subgrade Engineering Measures in Permafrost Regions*; Lanzhou University Press: Lanzhou, China, 2016; pp. 76–106.
19. Qin, Y.; Zhang, J. A review on the cooling effect of duct-ventilated embankments in China. *Cold Reg. Sci. Technol.* **2013**, *95*, 1–10. [CrossRef]
20. Song, Y.; Jin, L.; Zhang, J. In-situ study on cooling characteristics of two-phase closed thermosyphon embankment of Qinghai–Tibet Highway in permafrost regions. *Cold Reg. Sci. Technol.* **2013**, *93*, 12–19. [CrossRef]
21. Wang, S.; Jin, L.; Peng, H.; Chen, J.; Mu, K. Damage analysis of the characteristics and development process of thermosyphon embankment along the Qinghai-Tibet Highway. *Cold Reg. Sci. Technol.* **2017**, *142*, 118–131. [CrossRef]
22. Chai, M.; Li, G.; Ma, W.; Chen, D.; Du, Q.; Zhou, Y.; Qi, S.; Tang, L.; Jia, H. Damage characteristics of the Qinghai-Tibet Highway in permafrost regions based on UAV imagery. *Int. J. Pavement Eng.* **2022**, 1–12. [CrossRef]
23. Johansson, M.; Kerman, J.; Keuper, F.; Christensen, T.R.; Callaghan, L.T.V. Past and Present Permafrost Temperatures in the Abisko Area: Redrilling of Boreholes. *AMBIO* **2011**, *40*, 558–565. [CrossRef]
24. Ramos, M.; Hasler, A.; Vieira, G.; Hauck, C.; Gruber, S. Drilling and installation of boreholes for permafrost thermal monitoring on Livingston Island in the maritime Antarctic. *Permafr. Periglac.* **2010**, *20*, 57–64. [CrossRef]
25. Ma, S.; Yang, B.; Zhao, J.; Tan, C.; Chen, J.; Mei, Q.; Hou, X. Hydrothermal dynamics of seasonally frozen soil with different vegetation coverage in the Tianshan Mountains. *Front. Earth Sci.* **2022**, *9*, 806309. [CrossRef]
26. Yuan, C.; Yu, Q.; You, Y.; Guo, L. Deformation mechanism of an expressway embankment in warm and high ice content permafrost regions. *Appl. Therm. Eng.* **2017**, *121*, 1032–1039. [CrossRef]
27. Daanen, R.P.; Ingeman-Nielsen, T.; Foged, N.; Marchenko, S.S.; Svendsen, K.H. Permafrost degradation risk zone assessment using simulation models. *Cryosphere* **2011**, *5*, 1043–1056. [CrossRef]
28. Ni, J.; Wu, T.; Zhu, X.; Hu, G.; Zou, D.; Wu, X.; Li, R.; Xie, C.; Qiao, Y.; Pang, Q.; et al. Simulation of the Present and Future Projection of Permafrost on the Qinghai-Tibet Plateau with Statistical and Machine Learning Models. *J. Geophys. Res.-Atmos.* **2021**, *126*, jd033402. [CrossRef]

29. Filimonov, M.Y.; Kamnev, Y.K.; Shein, A.N.; Vaganova, N.A. Modeling the Temperature Field in Frozen Soil under Buildings in the City of Salekhard Taking into Account Temperature Monitoring. *Land* **2022**, *11*, 1102. [CrossRef]
30. Li, R.; Zhao, L.; Ding, Y.; Wu, T.; Xiao, Y.; Du, E.; Liu, G.; Qiao, Y. Temporal and spatial variations of the active layer along the Qinghai-Tibet Highway in a permafrost region. *Chin. Sci. Bull.* **2012**, *57*, 4609–4616. [CrossRef]
31. Zhang, M.; Lai, Y.; Dong, Y. Three-Dimensional Nonlinear Analysis for the Cooling Characteristics of Crushed-Rock Interlayer Embankment with Ventilated Duct along the Qinghai-Tibet Expressway in Permafrost Regions. *J. Cold Reg. Eng.* **2010**, *24*, 126–141. [CrossRef]
32. Fu, Z.; Wu, Q.; Zhang, W.; He, H.; Wang, L. Water Migration and Segregated Ice Formation in Frozen Ground: Current Advances and Future Perspectives. *Front. Earth Sci.* **2022**, *10*, 826961. [CrossRef]
33. Korte, S.; Gieschen, R.; Stolle, J.; Goseberg, N. Physical Modelling of Arctic Coastlines—Progress and Limitations. *Water* **2020**, *12*, 2254. [CrossRef]
34. Li, G.; Zhang, M.; Pei, W.; Melnikov, A.; Khristoforov, I.; Li, R.; Yu, F. Permafrost extent and active layer thickness variation in the Northern Hemisphere from 1969 to 2018. *Sci. Total Environ.* **2022**, *804*, 150182. [CrossRef]
35. Luo, J.; Niu, F.-j.; Lin, Z.-j.; Liu, M.-h.; Yin, G.-a. Variations in the northern permafrost boundary over the last four decades in the Xidatan region, Qinghai–Tibet Plateau. *J. Mt. Sci.* **2018**, *15*, 765–778. [CrossRef]
36. Wang, L.; Zhao, L.; Zhou, H.; Liu, S.; Du, E.; Zou, D.; Liu, G.; Wang, C.; Li, Y. Permafrost Ground Ice Melting and Deformation Time Series Revealed by Sentinel-1 InSAR in the Tanggula Mountain Region on the Tibetan Plateau. *Remote Sens.* **2022**, *14*, 811. [CrossRef]
37. Bai, L.R.; Chai, M.T.; Wu, L.B.; Zhang, X.Y.; Cao, J.S. Extraction and Analysis on Pavement Defects of the Qinghai-Tibet Highway. *Highway* **2021**, *66*, 32–37.
38. Luo, L.; Ma, W.; Zhao, W.; Zhuang, Y.; Zhang, Z.; Zhang, M.; Ma, D.; Zhou, Q. UAV-based spatiotemporal thermal patterns of permafrost slopes along the Qinghai–Tibet Engineering Corridor. *Landslides* **2018**, *15*, 2161–2172. [CrossRef]
39. Ye, L.; Li, F.; Huang, X.N. Application and Research of Comprehensive Geophysical Prospecting Technology in Permafrost Exploration of Northeast Highway Project. *J. Catastrophol.* **2018**, *33* (Suppl. 1), 25–29. [CrossRef]
40. Shan, W.; Xu, Z.; Guo, Y.; Zhang, C.C.; Hu, Z.G.; Wang, Y.Z. Geological methane emissions and wildfire risk in the degraded permafrost area of the Xiao Xing'an Mountains, China. *Sci. Rep.* **2020**, *10*, 21297. [CrossRef]
41. Zeng, Z.G.; Huang, Y.Z.; Xia, Z.Y.; Seguin, M.K. The Radar Detecting on Permafrost Distribution under the Asphalt Road of Qinghai-Xizang Highway. *J. Glaciol. Geocryol.* **1993**, *15*, 70–76.
42. Liu, L.B.; Qian, R.Y. Ground penetrating radar: A critical tool in neat-surface geophysics. *Chin. J. Geophys.* **2015**, *58*, 2606–2617. [CrossRef]
43. Solla, M.; Pérez-Gracia, V.; Fontul, S. A Review of GPR Application on Transport Infrastructures: Troubleshooting and Best Practices. *Remote Sens.* **2021**, *13*, 672. [CrossRef]
44. Ling, J.; Qian, R.; Shang, K.; Guo, L.; Zhao, Y.; Liu, D. Research on the Dynamic Monitoring Technology of Road Subgrades with Time-Lapse Full-Coverage 3D Ground Penetrating Radar (GPR). *Remote Sens.* **2022**, *14*, 1593. [CrossRef]
45. De Benedetto, D.; Barca, E.; Castellini, M.; Popolizio, S.; Lacolla, G.; Stellacci, A.M. Prediction of Soil Organic Carbon at Field Scale by Regression Kriging and Multivariate Adaptive Regression Splines Using Geophysical Covariates. *Land* **2022**, *11*, 381. [CrossRef]
46. Ballabio, C.; Panagos, P.; Lugato, E.; Huang, J.H.; Orgiazzi, A.; Jones, A.; Fernandez-Ugalde, O.; Borrelli, P.; Montanarella, L. Copper distribution in European topsoils: An assessment based on LUCAS soil survey. *Sci. Total Environ.* **2018**, *636*, 282–298. [CrossRef]
47. Pilecki, Z.; Krzysztof, K.; Elżbieta, P.; Andrzej, K.; Sylwia, T.-S.; Tomasz, Ł. Identification of buried historical mineshaft using ground-penetrating radar. *Eng. Geol.* **2021**, *294*, 106400. [CrossRef]
48. Núñez-Nieto, X.; Solla, M.; Gómez-Pérez, P.; Lorenzo, H. GPR Signal Characterization for Automated Landmine and UXO Detection Based on Machine Learning Techniques. *Remote Sens.* **2014**, *6*, 9729–9748. [CrossRef]
49. Fediuk, A.; Wunderlich, T.; Wilken, D.; Rabbel, W. Ground Penetrating Radar Measurements in Shallow Water Environments—A Case Study. *Remote Sens.* **2022**, *14*, 3659. [CrossRef]
50. Wu, T.; Wang, Q.; Zhao, L.; Du, E.; Wang, W.; Batkhishig, O.; Battogtokh, D.; Watanabe, M. Investigating internal structure of permafrost using conventional methods and ground-penetrating radar at Honhor basin, Mongolia. *Environ. Earth Sci.* **2012**, *67*, 1869–1876. [CrossRef]
51. Sjoberg, Y.; Marklund, P.; Pettersson, R.; Lyon, S. Geophysical mapping of palsa peatland permafrost. *Cryosphere* **2014**, *8*, 5137–5168. [CrossRef]
52. Wang, Y.; Jin, H.; Li, G. Investigation of the freeze–thaw states of foundation soils in permafrost areas along the China–Russia Crude Oil Pipeline (CRCOP) route using ground-penetrating radar (GPR). *Cold Reg. Sci. Technol.* **2016**, *126*, 10–21. [CrossRef]
53. Ma, W.; Mu, Y.H.; Xie, S.B.; Mao, Y.C.; Chen, D. Thermal-mechanical influences and environmental effects of expressway construction on the Qinghai-Tibet permafrost engineering corridor. *Adv. Earth Sci.* **2017**, *32*, 459–464. [CrossRef]
54. Wang, W. Research on the Disaster Mechanism and Preventive Measures of subgrade Defect in Permafrost Regions under the Double thermal effect of Sunny-Shady Slope and Roadside Lake. Master's Thesis, Chang'an University, Xi'an, China, 2021. [CrossRef]

55. Wang, S.; Li, Z.; Zhang, J.; Chen, J. *Highway Construction Technology on Permafrost Regions*; China Communications Press: Beijing, China, 2008; pp. 25–32.
56. Lin, Z. A new map of permafrost distribution on the Tibetan Plateau (2017). *Cryosphere* **2019**, *11*, 2527–2542. [CrossRef]
57. Davis, J.L.; Annan, A.P. Ground-Penetrating Radar for High-Resolution Mapping of Soil and Rock STRATIGRAPHY1. *Geophys. Prospect.* **1989**, *37*, 531–551. [CrossRef]
58. Blindow, N. Ground Penetrating Radar. In *Groundwater Geophysics: A Tool for Hydrogeology*; Kirsch, R., Ed.; Springer: Berlin/Heidelberg, Germany, 2006; pp. 227–252.
59. Shu, Z.L.; Liu, B.X.; Liu, X.R.; Zhu, C.H. *Forward and Inverse Theory and Signal Processing of Ground-Penetrating Radar*; Science Press: Beijing, China, 2017; pp. 1–10.
60. Zeng, Z.F.; Liu, S.X.; Wang, Z.J.; Xue, J. *Principle and Application of Ground-Penetrating Radar*; Science Press: Beijing, China, 2006; pp. 1–119.
61. Reflexw. *User Guide of Reflexw Computer Program*; Sandmeier Geophysical Research: Karlsruhe, Germany, 2018.
62. Benedetto, A.; Tosti, F.; Bianchini Ciampoli, L.; D'Amico, F. An overview of ground-penetrating radar signal processing techniques for road inspections. *Signal Process.* **2017**, *132*, 201–209. [CrossRef]